

Full length article

Microstructural evolution and phase transformation in twinning-induced plasticity steel induced by high-pressure torsion



X.H. An ^{a,*}, Q.Y. Lin ^a, G. Sha ^b, M.X. Huang ^c, S.P. Ringer ^{a,d}, Y.T. Zhu ^{b,e}, X.Z. Liao ^{a,**}

^a School of Aerospace, Mechanical and Mechatronic Engineering, The University of Sydney, Sydney, NSW 2006, Australia

^b School of Materials Science and Engineering, Nanjing University of Science and Technology, Jiangsu 210094, China

^c Department of Mechanical Engineering, The University of Hong Kong, Hong Kong, China

^d Australian Centre for Microscopy & Microanalysis, The University of Sydney, Sydney, NSW 2006, Australia

^e Department of Materials Science and Engineering, North Carolina State University, Raleigh, NC 27695, USA

ARTICLE INFO

Article history:

Received 9 December 2015

Received in revised form

5 February 2016

Accepted 19 February 2016

Available online 11 March 2016

Keywords:

Twinning-induced plasticity steel

Nanostructures

Phase transformation

Element diffusion and segregation

High-pressure torsion

ABSTRACT

The microstructural evolution of twinning-induced plasticity steel during high-pressure torsion (HPT) processing at 573 K was systematically evaluated. Due to the high processing temperature, the formation of a homogeneous nanostructure was primarily dominated by complicated dislocation and grain boundary activities in lieu of deformation twinning. Apart from the grain refinement process, phase transformation took place at late stages of deformation, resulting in the microstructural fingerprint of equiaxed nanograins with multiple phases in the steel. On account of remarkable elemental redistribution, the diffusion-controlled nature of the transformation was convincingly identified. During the transformation, although the cementite also initially formed, austenite eventually decomposed into ferrite and Mn-riched $M_{23}C_6$ carbide, implying that Mn is the pivotal alloying element for the transformation kinetics. Owing to the sluggish bulk diffusivity of Mn, it is proposed that a high density of defects, nanostructures and the HPT processing play a crucial role in promoting the elemental diffusion and segregation and in stimulating the phase transformation.

© 2016 Acta Materialia Inc. Published by Elsevier Ltd. All rights reserved.

1. Introduction

Bulk ultrafine-grained (UFG, < 1000 nm) and nanocrystalline (NC, < 100 nm) materials have been extensively explored over the last two decades due to their superior mechanical properties, including exceptionally high strength and hardness, excellent fatigue resistance and low-temperature superplasticity [1–5]. Severe plastic deformation (SPD) is among the most effective methods that can produce fully dense and contamination-free bulk UFG and NC materials [3–5]. By recourse to the SPD techniques, originally coarse-grained structures can be substantially refined to UFG or NC structures through a series of sophisticated grain refinement processes [3–5]. Comprehensive understanding of the fundamental mechanisms of SPD-induced microstructural evolution is crucial for achieving optimal mechanical properties of these materials via fine-tuning their microstructures.

It is well documented that dislocation activities and

deformation twinning are the two primary SPD-induced grain refinement mechanisms [3]. For materials in which dislocation slip is the dominant deformation mechanism, the SPD-induced microstructural evolution is mainly controlled by complicated dislocation activities that subdivide a large grain into many smaller volume elements through the formation of dislocation cells. With increasing plastic strain, the cell boundaries gradually evolve into low-angle and then high-angle grain boundaries (LAGBs and HAGBs, whose misorientation angles are below and above 15°, respectively) [6,7]. In contrast, refinement via deformation twinning involves the formation of a high-density of nanoscale twins in coarse grains and the subsequent transformation of two-dimensional twin lamellae structures into three-dimensional nanograins through extensive interactions between twin boundaries (TBs) and other defects (mainly dislocations) [8]. The final grain sizes after the refinement by the two mechanisms are generally in the range of submicrometer and nanometer, respectively [8,9]. In these bulk UFG and NC materials, there are a considerable fraction of LAGBs and a high density of dislocations resided in or near non-equilibrium HAGBs, which remarkably influence the thermal stability and mechanical properties of the materials [10–12].

* Corresponding author.

** Corresponding author.

E-mail addresses: anxianghai@gmail.com (X.H. An), xiaozhou.liao@sydney.edu.au (X.Z. Liao).

In addition to grain refinement, SPD processing can also lead to the formation of non-equilibrium solid solutions, disordering, amorphization, and phase transformations under high stress levels in various alloys [13–16]. For example, SPD can dissolve cementite in pearlitic steels through extensive C-dislocation interactions [13], promoting a reverse phase transformation from ferrite to austenite [14]. Although the reverted austenitic phase is unstable at room temperature, the long-distance diffusion of C atoms, stemmed from the decomposition of cementite, stabilizes to some extent the austenitic phase [14]. Therefore, alloying elements dissolved in the matrix phase play a significant role in SPD-induced microstructural evolution of engineering materials.

As a promising candidate for numerous industrial applications, twinning-induced plasticity (TWIP) steels with the austenitic phase have been extensively investigated since they possess excellent combination of high tensile strength and good ductility, which originates from their exceptionally large work-hardening rate [17–20]. It is generally recognized that the high work-hardening rate is closely related to the formation of deformation twins [19,20]. TBs act as effective barriers for dislocation motion to strengthen the materials and the increasing density of TBs with further straining results in a “dynamic Hall-Petch effect”. Additionally, the extensive interaction between the interstitial C atoms of C–Mn dipoles and dislocations produces a dynamic strain aging effects, also leading to high work-hardening rate [21]. Based on the traditional crystal plasticity theory, the activation of predominant deformation mechanism is mainly controlled by the stacking fault energy (SFE) [22], which is highly dependent on the chemical composition of TWIP steels. Until now, most researches concerning TWIP steels focused on the dependence of deformation mechanisms on their alloying elements and SFE [23–26], and the properties associated with microstructures [27–30]. Compared to other advanced steels [13,31–35], investigation on the microstructural response of TWIP steels to SPD processing is still limited [37,38]. However, fundamental exploration of the SPD-induced microstructural evolution of TWIP steels is important both scientifically, for the comprehensive understanding of the grain refinement processes in the engineering metallic materials, and technologically with respect to their energy absorption applications where high strain will be imposed on the steels.

In present work, high-pressure torsion (HPT), which is one of the most popular SPD techniques [39], was applied to process a TWIP steel at 573 K. The HPT-induced microstructural evolution was systematically studied in virtue of various advanced characterization methods, including X-ray diffraction (XRD), conventional electron backscatter diffraction (EBSD), scanning electron microscope-transmission Kikuchi diffraction (SEM-TKD) and transmission electron microscopy (TEM). During HPT processing, diffusional phase transformation surprisingly occurred via the decomposition of austenite into ferrite and carbides. To link the phase transformation and elemental diffusion, atom probe tomography (APT) was employed to analyze the elemental distributions before and after HPT processing.

2. Experimental procedure

2.1. Materials and processing

The original TWIP steel used in this investigation is a commercial product produced by Ansteel Co. Ltd. in China. The nominal chemical composition of the TWIP steel is Fe-17.37Mn-3.31C-3.34Al-0.94Si in at.% or Fe-18Mn-0.75C-1.7Al-0.5Si in wt.%. Detailed information about the material is available in Refs. [40,41]. For HPT processing, the fully recrystallized steel was cut into disc samples with a diameter of 20 mm and a thickness of 1.5 mm. The

disks were HPT processed through 1, 5, 10, and 12 revolutions (thereafter referred to as 1R, 5R, 10R and 12R samples, respectively) under a quasi-constrained condition [39] with an imposed pressure of 4.0 GPa at 573 K. Before HPT processing, the anvils were pre-heated to 573 K and then held for 5 min to warm the samples. The temperature was kept at 573 ± 10 K during the process. The samples were quenched into water immediately after HPT processing. One or two revolutions of HPT were carried out for one time and above-mentioned procedure was repeated to reach the designed revolution numbers.

2.2. Materials characterization techniques

After HPT, disks with a diameter of 3 mm for microstructural characterization were taken near the edge of the HPT samples and were mechanically polished using 1200–4000 grit SiC papers sequentially to acquire a flat and smooth surface. All structural characterization experiments were undertaken at positions of ~1–2 mm away from the edge of disks and all micrographs were taken from plan-view. For XRD and conventional EBSD experiments, electro-polishing was conducted to remove the strained layer caused by mechanical polishing using a Struers LectroPol-5 unit and an electrolyte of 23% perchloric acid and 77% acetic acid under the voltage of 20 V at the ambient temperature for 50 s. XRD measurements of all specimens were performed using a Siemens D5000 diffractometer to identify the phase information of the steel before and after HPT. EBSD analysis of the original, 1R and 5R samples were carried out using a Carl Zeiss Ultra Plus field emission gun SEM with the operating voltage of 12 kV and the step sizes of 200 nm, 100 nm and 60 nm, respectively.

For the 10R and 12R samples with much finer microstructures, SEM-TKD and TEM were applied to characterize the microstructures and phase transformation. The samples were electropolished using a Struers TenuPol-5 jet electropolishing unit and a solution of 23% perchloric acid and 77% acetic acid under an operating voltage of 20 V and at a temperature of -20 °C. SEM-TKD experiments were performed in the Zeiss Ultra SEM with operating voltage of 20 kV and the step size of 10 nm. The detailed experimental set-up of SEM-TKD follows that presented in Ref. 42. The chemistry information of the samples was simultaneously collected using an Oxford Instruments AZtec EDS system with an X-Max 20 mm² silicon drift detector during the SEM-TKD mapping. TEM characterization was performed using a JEOL 2200F operating at 200 kV and a JEOL 3000F at 300 kV.

A local electrode atom probe was employed to acquire high-resolution compositional data of the coarse-grained sample and a 12R sample. Tip samples for APT analysis were prepared using a two-step electropolishing procedure with thin bars having cross-sections of 0.5×0.5 mm². The first step used an electrolyte of 25% perchloric acid in acetic acid at 15 V and the second step used an electrolyte of 4% perchloric acid in 2-butoxyethanol at 20 V. APT characterization was performed in an atom probe, CAMECA LEAP 4000X Si at a specimen temperature of 20 K under a laser pulse at an energy of 40 pJ and with a target evaporation rate of 1%. Reconstruction and quantitative analysis of atom probe data were performed by using IVAS 3.6.6 software.

3. Experimental results

3.1. XRD results before and after HPT

XRD patterns of the original steel and HPT samples are presented in Fig. 1. Within the XRD detection limit, only peaks from the austenitic phase were identified in the initial TWIP steel and the 1R and 5R samples. Although significant HPT-induced martensitic

transformation at room temperature has been reported in a TWIP steel [37], no martensite formed in the present study, which may be attributed to the high processing temperature suppressing the martensitic transformation. With further deformation, the (110) peak of ferrite (thereafter referred to as $(110)_\alpha$) is clearly detected in the 10R sample, signaling the phase transformation from austenite to ferrite. The $(110)_\alpha$ peak is more remarkable and the $(211)_\alpha$ peak is also notably identified in the 12R sample. Based on the XRD results, the volume fraction of ferrite is ~5.6% and ~20% in the 10R and 12R samples, respectively. It is well known that stress-induced martensitic transformation can be activated by mechanical loading, since austenite in the TWIP steel is metastable [25,28,37]. However, there was no report concerning deformation-induced phase transformation from austenite to ferrite. To comprehensively understand the HPT-induced microstructural evolution and phase transformation of the TWIP steel, in-depth microstructural investigations were performed by recourse of extensive EBSD and TKD characterization.

3.2. EBSD and TKD investigations of HPT-induced microstructural evolution

The original TWIP steel is of a recrystallized microstructure with an average grain size of ~4 μm and only a few LAGBs, as shown in Fig. 2 (a). In line with the XRD result, the phase map in Fig. 2(b) further confirms that the original TWIP steel contains only austenite. After HPT for 1 revolution, the original grain features including their shape and GBs were still traceable although there is gradual variation in the crystallographic orientations within individual grains, while a high density of LAGB with a fraction of ~68% formed within the grains, as exhibited in Fig. 3 (a–c). Larger changes in orientation are adjacent to GBs and near triple junctions, which stemmed from abundant dislocation activities, leading to the formation of LAGBs [7,43]. Fig. 3 (a) also reveals a few deformation twins, with TBs presented with red lines, in several grains whose orientations may favor deformation twinning [44,45]. No phase transformation was observed and only austenite existed in the sample (Fig. 3(b)). Usually, profuse twinning activities play a crucial role in accommodating the plastic strain imposed on the TWIP [23–30]. In the present investigation, dislocation slip rather than twinning was the dominant mechanism for the large shear deformation because of the high processing temperature, which will be

discussed in detail later.

HPT processing for 5 revolutions led to significant change in the microstructure. As exhibited in the orientation map in Fig. 3 (d), grains were strongly elongated with roughly parallel lamellar boundaries, interweaved with some nearly equiaxed ultrafine grains. The average width of the lamellar structure is ~1 μm . The phase map of Fig. 3 (e) shows only the austenitic phase in the sample. Compared to the 1R sample shown in Fig. 3 (c), the fraction of LAGB in the 5R sample was slightly reduced but was still as high as ~60%, while the density of deformation twins decreased as well based on the volume fraction of TBs, as illustrated in Fig. 3 (f). This could be ascribed to the detwinning behavior due to the extensive interaction between dislocations [35] and TBs and the twinning activation becomes increasingly difficult with the grain refinement in the micrometer range [44].

Owing to the limited spatial resolution of the conventional EBSD method, the microstructure characterization of the 10R and 12R samples was carried out by recourse of the SEM-TKD technique [42]. After HPT for 10 revolutions, although many grains are still elongated, the aspect ratios of grain length to width were prominently reduced, while the number of equiaxed ultrafine and nanoscale grains increased remarkably, as exhibited in Fig. 4 (a–c). In parallel with the XRD results, new phases with small grain sizes are detected in some “band-like” narrow local regions, as revealed in the phase map in Fig. 4 (c). Based on the Kikuchi patterns, the new phases are determined as ferrite and two types of carbides – cementite and M_{23}C_6 – with volume fractions of ~5.2%, 1.2% and 1.5%, respectively. Because of their small volume fractions, carbides were not identified by XRD. Although the experimental set-up of TKD and the nature of thin foil specimens make it difficult to collect compositional information with high accuracy [42], the inhomogeneous elemental distributions of Fe and Mn at places where the new phases formed were still identified, as shown in Fig. 4 (d) and (e), indicating clearly the diffusional nature of the phase transformation. Thus, elemental diffusion and redistribution play a crucial role in the phase transformation, which is significantly different from the martensitic transformation in TWIP steels [25,28,37].

The grain size distributions of austenite and ferrite in the 10R sample are shown in Fig. 5 (a) and (b), respectively. The average grain size of austenite and ferrite was ~130 nm and ~65 nm, respectively, and the latter had a narrower grain size distribution range. The grain sizes of two carbides were ~50 nm Fig. 5 (c) and (d) present the misorientation angle distribution of austenite and ferrite, respectively. Compared to 1R and 5R samples, the volume fraction of LAGBs in austenitic grains is remarkably decreased to ~26%, while there are only a few LAGBs with a fraction of ~10% in ferrite phase. In fact, although plenty of ultrafine and nanoscale grains were formed in many regions, combined with the significant reduction of LAGBs and the occurrence of the phase transformation, the microstructure of the steel was quite inhomogeneous even after HPT for 10 revolutions.

After HPT for 12 revolutions, the representative microstructural trait of the steel was uniformly distributed equiaxed nanograins, as detected in Fig. 6 (a–c). Meanwhile, the phase transformation proceeded, resulting in the formation of more ferrite and M_{23}C_6 carbide. However, the cementite phase was barely noticeable as shown in Fig. 6 (c). Based on the TKD result, the volume fractions of ferrite and M_{23}C_6 increased remarkably to 23% and 3.2%, respectively. Accompanied with the occurrence of extensive phase transformation, the distributions of Fe and Mn became increasingly inhomogeneous owing to the significant elemental redistribution, as exhibited in Fig. 6 (d) and (e). Qualitatively, the Mn-enriched and -depleted regions roughly correspond to the M_{23}C_6 carbide and ferrite, respectively, in which Fe is

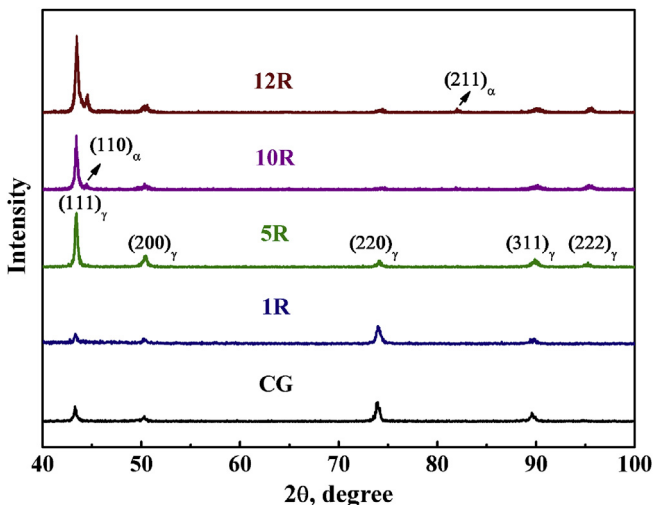


Fig. 1. XRD patterns of the original TWIP steel and those after different numbers of revolutions of HPT processing.

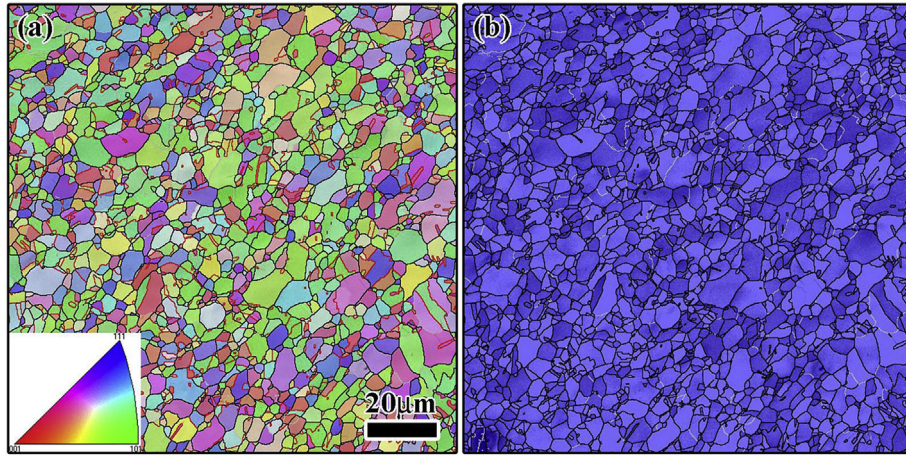


Fig. 2. (a) The orientation map of the CG TWIP steel and inserted image is the inverse pole figure (the black and white lines means the HAGB and LAGB, respectively); (b) The EBSD phase map of CG TWIP showing the fully austenite microstructure.

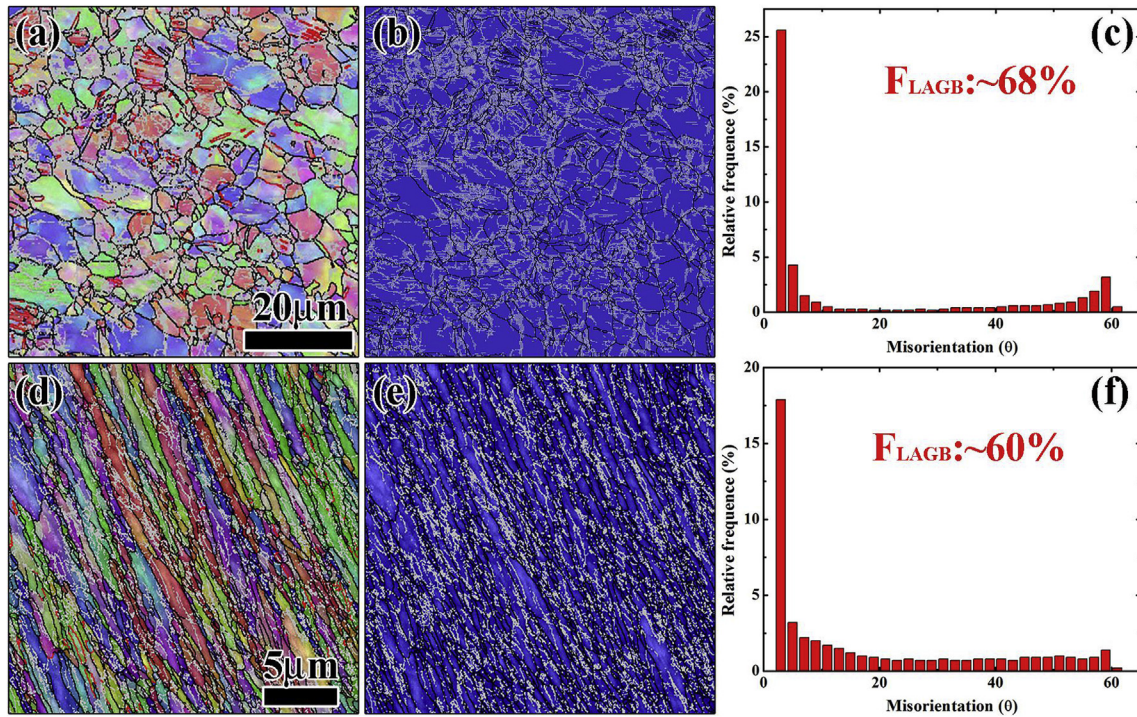


Fig. 3. After 1-revolution HPT: (a) EBSD orientation map (the red lines mean TBs); (b) the phase map; (c) misorientation angle distribution of the TWIP steel; After 5-revolutions HPT: (d) EBSD orientation map; (e) the phase map; (f) misorientation angle distribution of the TWIP steel. (For interpretation of the references to colour in this figure legend, the reader is referred to the web version of this article.)

reversely lean and enriched. Moreover, the average austenite grain size of ~ 135 nm was almost the same as that in the 10R sample, while the grain size of ferrite phase remarkably increased to ~ 115 nm, as revealed in Fig. 7 (a) and (b). The average grain size of $M_{23}C_6$ carbide increased slightly to ~ 60 nm. Thus, instead of grain refinement, grain growth occurred for ferrite and $M_{23}C_6$ and the total amounts of the new phases increased with deformation. In addition, the volume fraction of LAGBs in austenite further decreased to $\sim 21\%$, as illustrated in Fig. 7 (c). Differently, Fig. 7 (d) shows that the volume fraction of LAGBs in ferrite phase was $\sim 11\%$, which is about the same as that of the 10R sample.

3.3. TEM investigation on the microstructures of the 10R and 12R samples

Various dislocation configurations including dislocation cells and elongated subgrain boundaries are the characteristics of the inhomogeneous microstructures in many regions of 10R sample, interspersed with several isolated nanograins, as marked by arrows in Fig. 8 (a). Corresponding selected area electron diffraction (SAED) patterns confirm that only austenite exists in these areas. In contrast, many equiaxed ultrafine and nanoscale grains can be found in some local places, as exhibited in Fig. 8(b), while there are

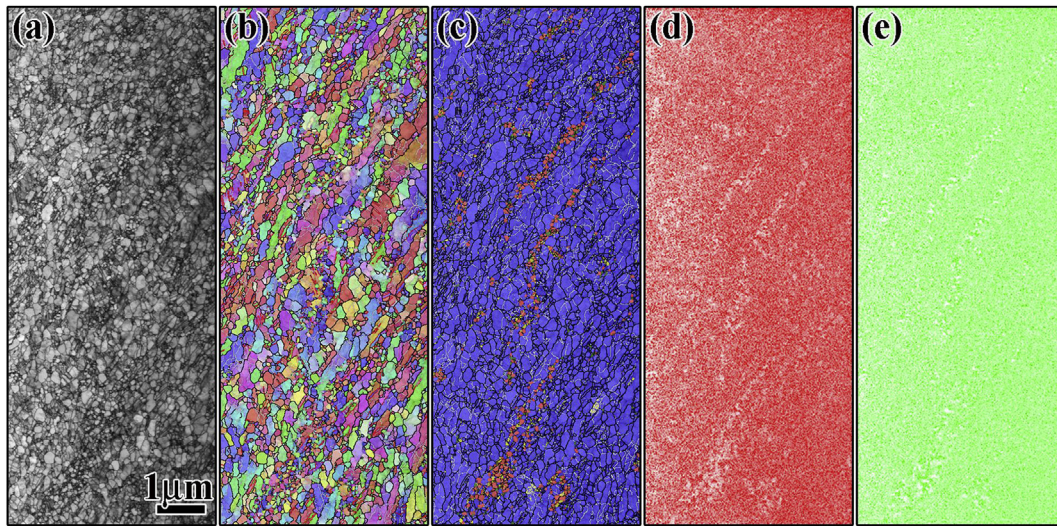


Fig. 4. (a) TKD pattern quality map of the TWIP steel after 10-revolutions HPT; (b) TKD orientation map; (c) TKD phase map with austenite in blue, ferrite in red, cementite in green and $M_{23}C_6$ carbide in yellow, implying the occurrence of phase transformation; (d) and (e) EDS element maps showing Fe and Mn $K\alpha$ X-ray counts, respectively. (For interpretation of the references to colour in this figure legend, the reader is referred to the web version of this article.)

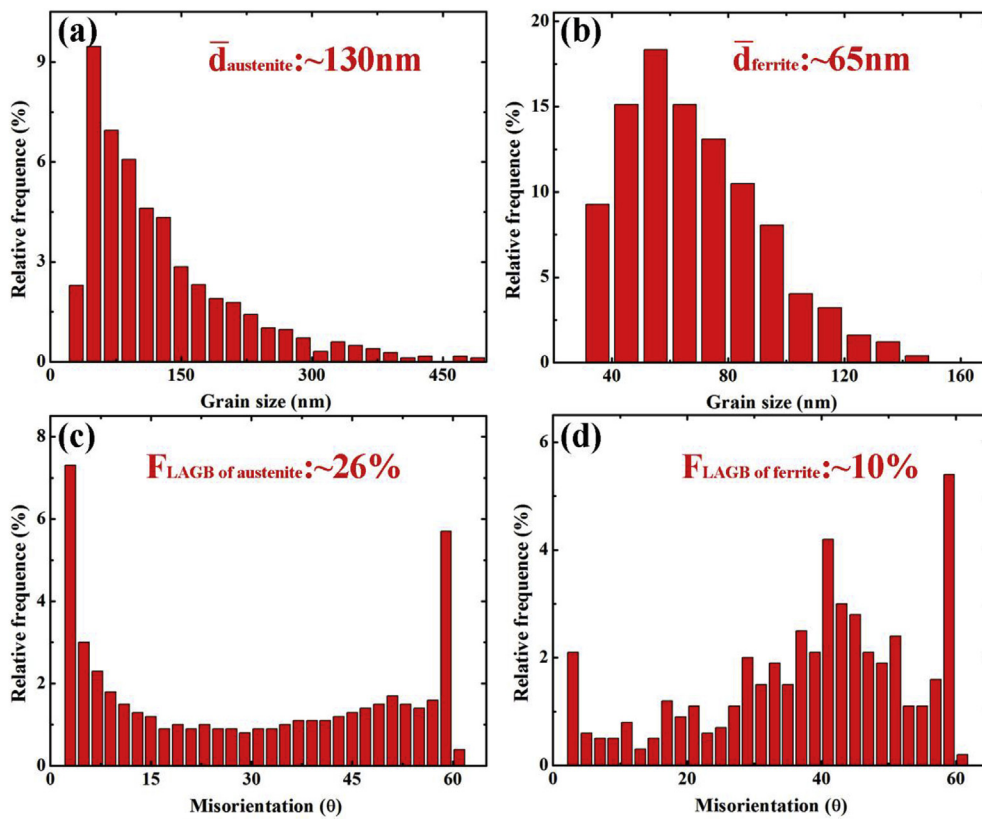


Fig. 5. (a) and (b) Grain size distributions of austenite and ferrites in the TWIP steel after 10-revolutions HPT, respectively; (c) and (d) misorientation angle distributions austenite and ferrites in the TWIP steel after 10-revolutions HPT, respectively.

still apparent dislocation substructures in the ultrafine grains, most of which are the austenitic phase. SAED patterns obtained from these zones, as inserted in Fig. 8 (b), validate the existence of multiple phases, indicating that the phase transformation took place. According to the SAED patterns, besides the austenite phase, the ferrite phase can be readily recognized as well, while several isolated spots, originated from carbides, are difficult to be

accurately indexed. Nevertheless, through indexing the SAED patterns of many individual grains, apart from the austenite and the ferrite, cementite and $M_{23}C_6$ carbide were efficaciously identified. Fig. 8 (c–e) presents typical morphologies and SAED patterns of ferrites, cementite and $M_{23}C_6$, respectively.

After HPT for 12 revolutions, NC grains with equiaxed morphology are the predominant microstructural signature of

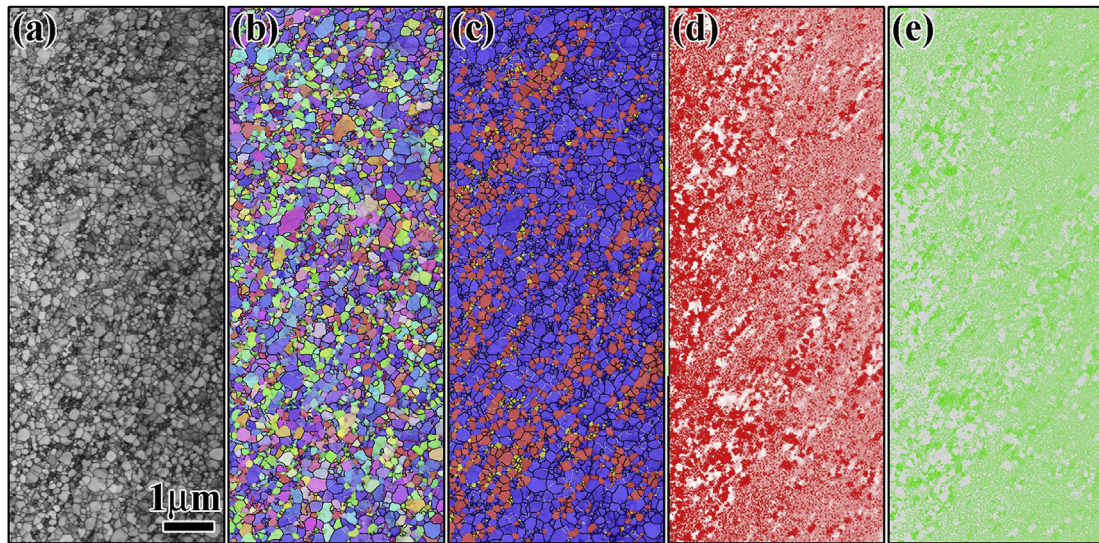


Fig. 6. (a) TKD pattern quality map of the TWIP steel after 12-revolutions HPT; (b) TKD orientation map; (c) TKD phase map with austenite in blue, ferrite in red and $M_{23}C_6$ carbide in yellow; (d) and (e) EDS element maps showing Fe and Mn $K\alpha$ X-ray counts, respectively. (For interpretation of the references to colour in this figure legend, the reader is referred to the web version of this article.)

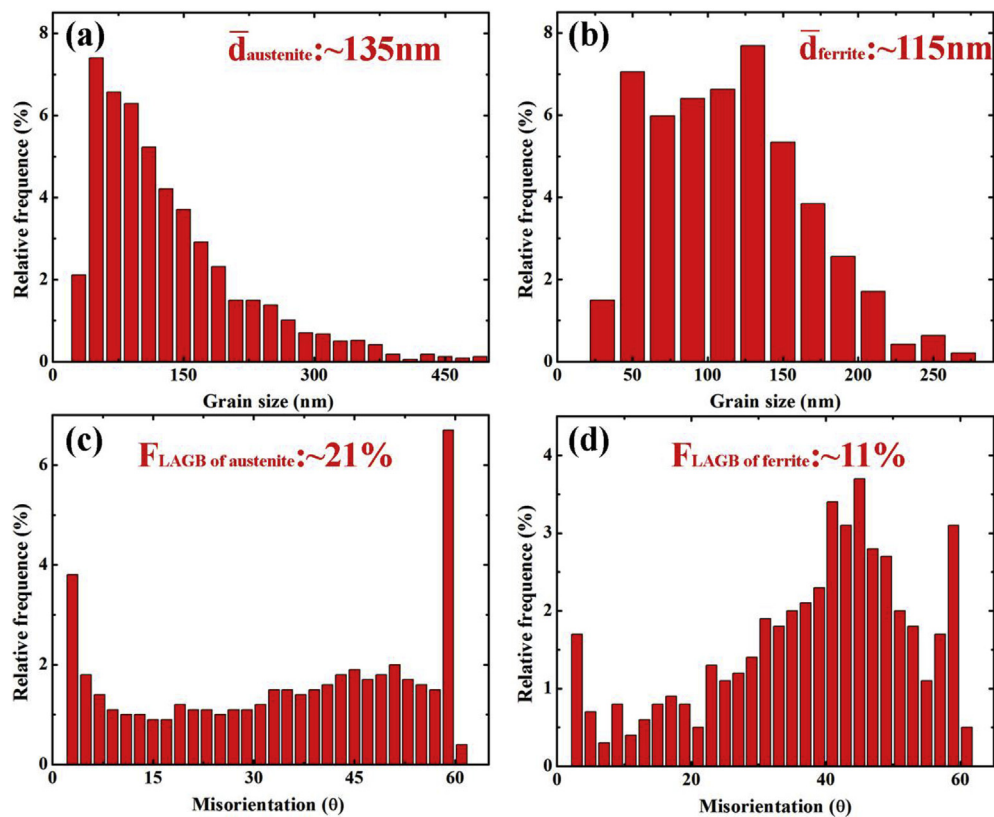


Fig. 7. (a) and (b) Grain size distributions of austenite and ferrites in the TWIP steel after 12-revolutions HPT, respectively; (c) and (d) misorientation angle distributions austenite and ferrites in the TWIP steel after 12-revolutions HPT, respectively.

the steel in most regions, as shown in Fig. 9 (a) and (b). The corresponding SAED pattern inserted in Fig. 9 (a) identifies three phases, i.e., austenite, ferrite and $M_{23}C_6$ carbide. No cementite was found. Typical atomic-scale TEM images and their corresponding fast Fourier transformation (FFT) patterns of austenite, ferrite and $M_{23}C_6$ carbides are shown in Fig. 9 (c)–(e). While the GBs in SPD materials processed at the ambient temperature are

usually blurred due to the significant internal stress and limited dynamic recovery [8,35,46], most GBs in present study are quite clear, as exhibited in Fig. 9 (a) and (b), implying that dynamic recovery or recrystallization caused by the high processing temperature, play an essential role in shaping the morphology of these fine grains. A few deformation twins were occasionally found in austenitic nanograins and $M_{23}C_6$ carbides. Some

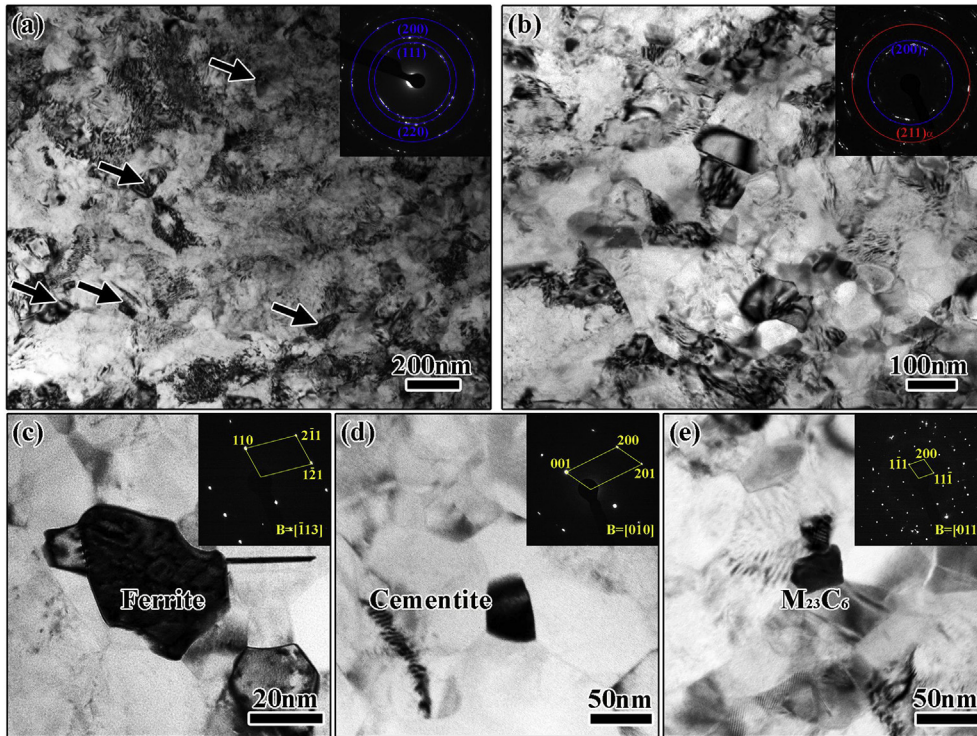


Fig. 8. (a) and (b) Typical TEM images of the TWIP steel after 10-revolutions HPT, showing the only austenite and multiple phase microstructures, respectively and the inserted images are corresponding SEAD patterns; (c–e) typical morphology of ferrite, cementite and $M_{23}C_6$ carbide with their SEAD patterns, respectively.

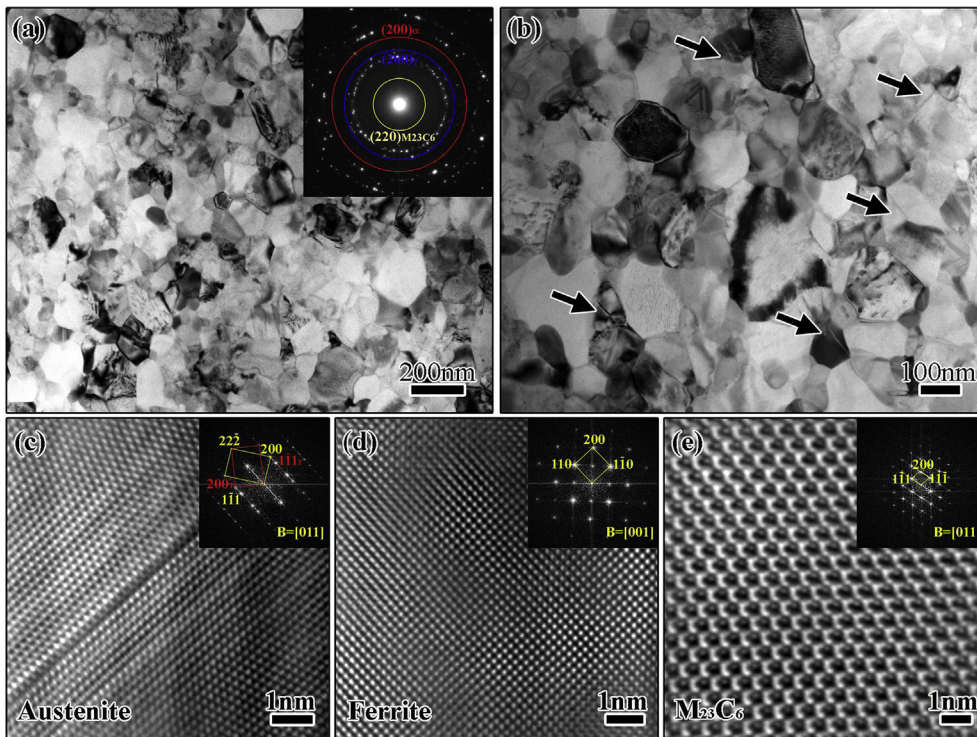


Fig. 9. (a) and (b) Characteristic TEM images and the SEAD patterns of the TWIP steel microstructures after 12-revolutions HPT and the deformation twins are marked by the arrows in (b); (c–e) HRTEM images and corresponding FFT of austenite, ferrite and $M_{23}C_6$ carbide, respectively.

twinned grains are marked by arrows in Fig. 9 (b). These twins are expected to form via partial dislocation emissions from GBs [47,48]. In a whole, the microstructure in the 12R sample is quite homogeneous in comparison to that in the 10R sample.

3.4. APT investigations of elemental distribution in the original steel and the 12R sample

Based on the SEM-TKD results, the phase transformation in the

present investigation is diffusion controlled. Therefore, information on the elemental distributions before and after transformation is crucial for comprehensive understanding of the phase transformation. Fig. 10 exhibits the typical APT results of the original TWIP steel. Detailed elemental concentrations are summarized in Table 1. The concentrations of Mn and Si are slightly higher, while the contents of C and Al are lower than the nominal compositions. All elements are uniformly distributed without apparent segregation, validating a single-phase with randomly distributed solutes in the original steel. In contrast, as revealed in the APT maps in Fig. 11, inhomogeneous elemental distribution existed after HPT for 12 revolutions. The segregation of the Mn and C atoms is more severe than that of Si and Al. This further substantiates the diffusional nature of the phase transformation.

Referring to the EDS results, the C and Mn-enriched regions identified by iso-concentration surfaces is $M_{23}C_6$ carbide, while the Mn-depleted zone is recognized as ferrite, as shown in Fig. 12 (a) and (b). One-dimensional compositional profiles across ferrite, carbide and austenite, as illustrated in Fig. 12 (c–e), are used to quantify the elemental distribution in these phases. The apparent compositional variation in ferrite, carbide and austenite is clearly discernable. The compositions of the three phases are listed in Table 1. As revealed in Fig. 12 (d) and (e), Mn partitioned more strongly into the austenitic phase, but Fe partitioned more strongly into the ferrite while Si and Al showed no clear partitioning between the two phases. The C concentration in ferrite is ~ 0.56 at.%, which is higher than that in conventional α -Fe (< 0.1 at.%) [14]. In fact, the C content in austenite is also decreased to ~ 1.0 at.%, lower than that in the original TWIP steel, while Fe and Mn contents in austenite slightly increased and decreased, respectively, after HPT processing. In the $M_{23}C_6$ carbide, the enrichment of Mn and C and the leanness of Fe and Si are remarkable. The minimum of Si at the center of the $M_{23}C_6$ carbide is attributed to the diminishing equilibrium solubility of Si in carbides [49]. However, the C content of ~ 11.5 at.% is lower than the typical stoichiometric value of 20.6 at.% in $M_{23}C_6$ carbide. Both Mn and C are well-known austenite stabilizers and Mn is also a carbide-forming element [23,49]. In association with the prominent segregation of Mn and C atoms, the phase transformation should be intimately correlated to the diffusion of these two elements, resulting in the decomposition of austenite to ferrites and carbides.

4. Discussion

After HPT processing, the original coarse grains of the TWIP

steel were substantially refined, leading to the formation of homogeneously distributed equiaxed nanograins, while the phase transformation at later stages of deformation endues the nanostructure with multiple phases in lieu of the initially single austenitic phase. Different from early studies about the deformation-induced martensitic transformation in TWIP steels [25,28,37], herein, phase transformation involves significant elemental redistribution via diffusion, which was promoted by the nanostructures and HPT processing. In this section, the microstructural evolution and phase transformation of the TWIP steel will be discussed in detail.

4.1. HPT-induced microstructural evolution

As mentioned above, SPD-induced microstructural evolution is highly dependent on the dominant deformation mechanism, which is controlled by the SFE [3,45]. Deformation twinning is the favorable deformation mechanism for TWIP steels with SFE in the range of $18\text{--}45$ mJ m $^{-2}$ [23]. The SFE of steels can be finely manipulated through appropriate adjustment of the types and concentrations of alloying elements [18,24–26]. However, processing temperature is another factor that affects significantly the deformation behavior of materials [23,30]. While low temperature favors deformation twinning, high temperature promotes dislocation slip [23,30]. It has been shown that the plastic deformation was mainly accommodated by the dislocations rather than twinning during warm rolling at 573 K in the same TWIP [41]. Therefore, different from the early studies on the twinning structure evolution of TWIP steels during SPD [35–37], dislocation activities dominate the formation of HPT-induced nanostructures in the present study due to the high processing temperature [23,30].

The microstructure evolution during HPT can be roughly divided into four steps, which are outlined schematically in Fig. 13. During early stages of deformation (step 1), the original grain morphology is still detectable and grain interior accommodates the major shear strain since the GB regions are relatively “strong”. Profuse LAGBs with high-density dislocations accumulate drastically within the grains and near the GBs, causing gradual variation of crystal orientation within the original individual grains, as detected in Fig. 3(a). It has to be mentioned that the characterized regions in Fig. 3 (a) were subjected to the von Mises strain ϵ of about 40 ($\epsilon = 2\pi Nr / \sqrt{3}h$, where r and h are the radius and thickness of the disk, respectively, and N is the number of revolutions), while areas with strain smaller than 40 present not much difference in morphology but do show lower dislocation densities and lower

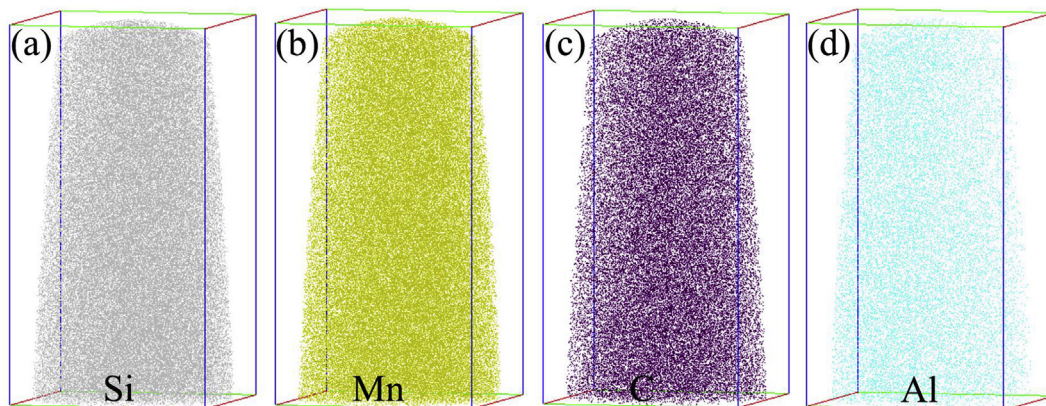
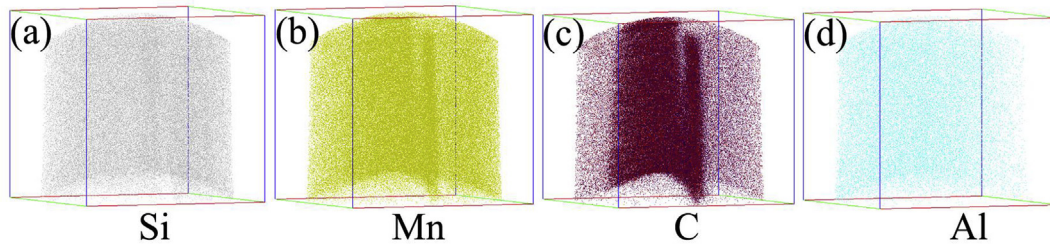
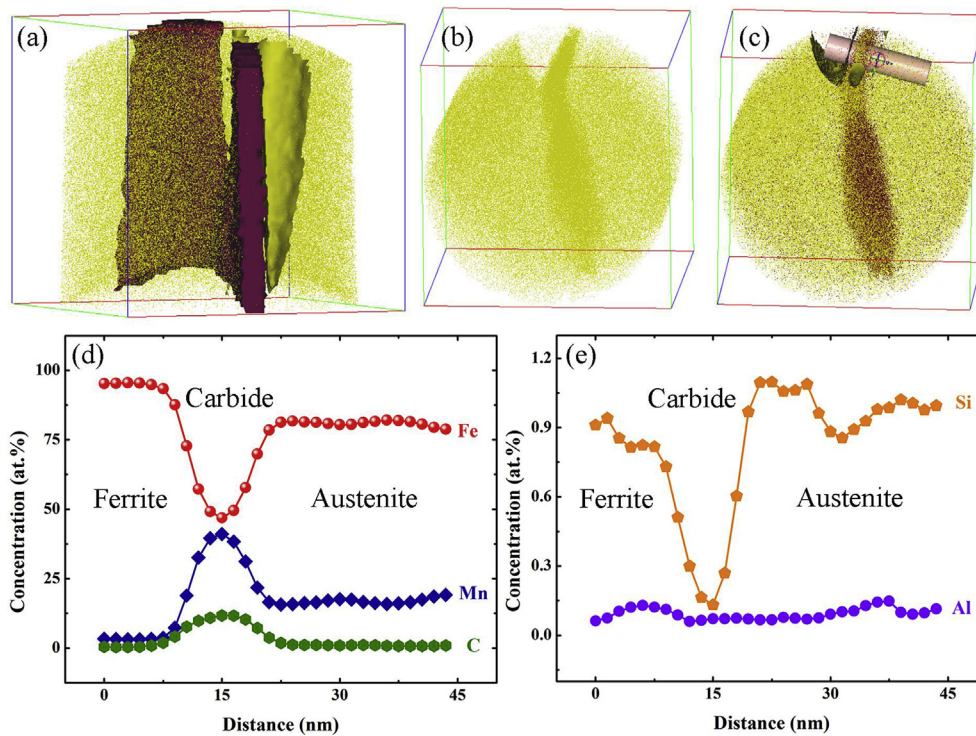


Fig. 10. 3D atom map of alloying elements of the original TWIP steel: (a) Si, (b) Mn, (c) C, (d) Al, exhibiting the homogeneous distribution of these elements (Box dimension: 58 nm \times 58 nm \times 110 nm).

Table 1APT results of the chemical compositions of the original TWIP steel and the austenite, ferrite and $M_{23}C_6$ carbide obtained after 12-revolutions HPT.

Materials	Phases	Fe (at%)	Mn (at%)	C (at%)	Si (at%)	Al (at%)
Original TWIP steel	Austenite	77.65	18.26	2.95	0.98	0.16
TWIP steel after 12-revolutions HPT	Austenite	80.51	17.53	1.03	0.85	0.08
	Ferrite	95.21	3.18	0.56	0.95	0.10
	$M_{23}C_6$ Carbide	48.56	39.66	11.53	0.18	0.07

**Fig. 11.** 3D atom map of alloying elements of the TWIP steel after 12-revolutions HPT: (a) Si, (b) Mn, (c) C, (d) Al, revealing the segregations of these elements (Box dimension: 105 nm × 105 nm × 100 nm).**Fig. 12.** (a) and (b) 3D maps of C and Mn with isosurfaces of a C-rich region and Mn-lean region, defined at 8 at% C and 10 at% Mn, respectively for the TWIP steel after 12-revolutions HPT; (c) 3D maps of C and Mn with isosurfaces defined at 8 at% C and 10 at% Mn and 1D concentration files are drawn along the bar; (d) the corresponding 1D concentration profiles of Fe, Mn and C, which helps distinguish the austenite, ferrite and $M_{23}C_6$ carbide; (e) the corresponding 1D concentration profiles of Al and Si.

volume fractions of LAGBs. Generally, such high strain readily induces the severe deformation of the GBs [7,43,46]. In the present study, large amounts of alloying elements in the TWIP steel, especially the C–Mn dipoles, could decrease GB energy and moving velocity, and drag or suppress the GB motion [22,50]. With further deformation, various defects are increasingly stored within grains, making the grain interior and GB comparably “strong”. Accordingly, GBs begin to play crucial roles in carrying the plastic strain during step 2 of the deformation, while the grains are prominently elongated and the grain thickness is apparently reduced. However, the thickness of elongated grains cannot be continuously decreased [7].

During the deformation in step 3, some microscale shear bands formed in several regions due to the large strain or stress localization. These bands penetrate GBs and cut the elongated grains, leading to formation of roughly equiaxed nanograins within the bands. Besides, LAGBs evolve gradually into HAGBs via generation, deposition and recombination of more dislocations [6], which causes the notable reduction of grain length and the remarkable decrease in the volume fraction of LAGBs. During step 4, these processes are progressively proceeded, while HAGBs are significantly sharpened so that they are clearly recognizable through boundary migration and dynamic recovery favored by the high

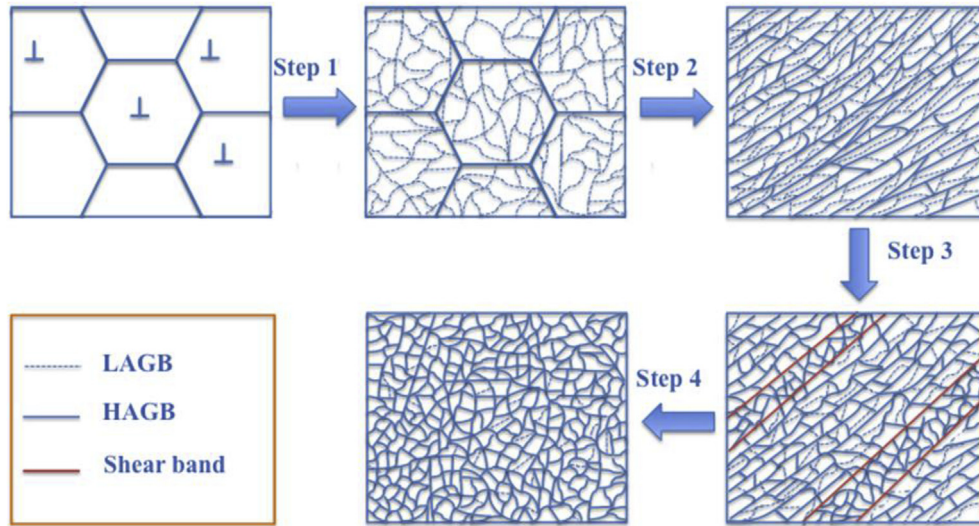


Fig. 13. A schematic diagram of the HPT-induced microstructure evolution of the TWIP steel.

processing temperature. Finally, the equiaxed nanoscale grains with uniform distribution become the representative trait of microstructures in TWIP steel.

It is referred above that alloying elements redistributed extensively during HPT that led to diffusional phase transformation, which also affected remarkably the nanostructural evolution. Compared to those imposed on various materials to achieve uniformly distributed nanograins [7,42,45], ultra-high von Mises strain of ~500 is herein required. The dramatic segregation of elements in or near dislocations and GBs essentially slows down the dislocation recovery and subgrain boundary migration, which are crucial for the formation of nanograins [7,46,51]. In contrast, the occurrence of the phase transformation actually benefits the grain refinement. Firstly, the nanoscale ferritic grains and carbides directly formed via the decomposition of the austenite phase. Secondly, owing to the variations of the microstructures and properties among these phases, large strain or stress incompatibility exists near their inter-phase boundaries, leading to additional accumulation of dislocations to accelerate the formation of nanostructures [3–5,35]. As shown in Fig. 4 (b) and (c), equiaxed austenitic nanograins are readily detected in the regions near ferrite and carbides, while austenitic grains elsewhere were still elongated. Therefore, the mutual interaction of the grain refinement and phase transformation during SPD promotes a homogeneous nanostructure with multiple phases.

4.2. HPT-induced phase transformation

Although the metastable austenite in the TWIP steel can transform into martensite through a stress-induced transformation process [17,18,25,28,37], diffusional phase transformation is herein preferred, on account of the significant diffusion of alloying elements as shown in Figs. 11 and 12. In principle, the diffusional transformation is primarily activated by the thermally activated atomic diffusion at sufficiently high temperatures [52]. A recent investigation uncovered that isothermal aging at 773–873 K for tens of hours led to a partial phase transformation from austenite to pearlite in a TWIP steel with 14% Mn content and that Mn partitioning is the key for the transformation [53]. Our HPT processing temperature was only 573 K and the duration of HPT samples staying at the temperature was less than an hour, which is not enough to stimulate the diffusional phase transformation without

deformation due to the sluggish bulk diffusivity of Mn atoms [52]. Therefore, it is expected that a high density of defects, including vacancies, dislocations and GBs introduced by HPT processing, played an essential role in promoting the elemental diffusion and triggering the decomposition of austenite into ferrite and carbides.

Figs. 11 and 12 indicate the inhomogeneous distribution of Mn and C atoms after HPT, substantiating the diffusional transformation nature. As an interstitial solute in iron lattice, C can easily diffuse for a long distance even at room temperature [14,50]. In contrast, Mn is a substitutional solute with very low bulk diffusivity. For example, the diffusion distance of Mn is only ~0.5 nm in ferrite at 673 K for 30 min [50] and ~5 nm in austenite at 823 K °C for 10 h [53]. Accordingly, the diffusion of Mn at 573 K for ~35–42 min should usually be negligible. However, the introduction of a high density of defects, including vacancies, dislocations and LAGBs, by HPT provides rapid diffusion channels for solute atoms, which increases their diffusion coefficients [14,49,50,52]. Besides, dislocations and GBs provide preferred nucleation sites for the formation of new phases, leading to their apparent segregation [54,55]. Significant segregation at defects changes the local chemical equilibrium and then the difference in the Gibbs free energies of parent and new phases, offering the chemical driving force for the phase transformation [52]. Meanwhile, the large external stress and strain localization facilitate the nucleation of ferrites and carbides [14,55]. As shown in Fig. 14 (a), the decomposition of austenite occurred in a highly localized shear band, evidenced by the formation of the $M_{23}C_6$ carbide in Fig. 14 (b) and (c). This explains why most of the newly formed ferrite and carbides present the “band-like” distribution at the early stages of phase transformation, as revealed in Fig. 4 (c). It is well known that Mn is a carbide-forming element and its solubility in carbides is much higher than that in ferrite [50,54]. After the nucleation of new phases, the significantly different solubility yields a thermodynamic driving force that promotes diffusion of Mn along the subgrain boundaries or triple junction into carbide nuclei [50]. With further deformation, the segregation and partitioning of Mn and C atoms are more remarkable, while the formation of nanograins also benefits the diffusion process due to the reduced length scale, both of which increase the kinetics of the transformation and the growth of ferrite and carbides. Therefore, the grain sizes of ferrites and carbides increased during HPT in lieu of the grain refinement.

In the recent investigation, no new phases formed during warm

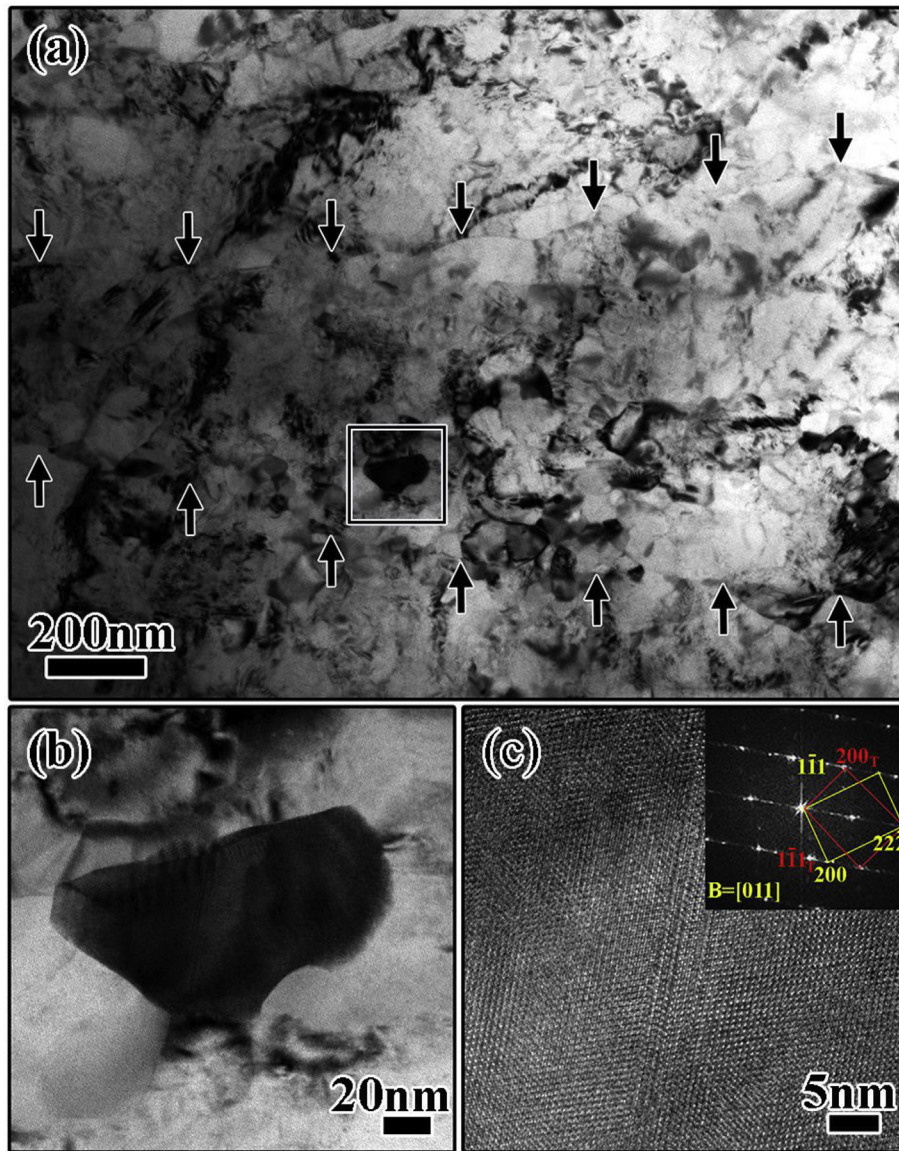


Fig. 14. (a) The phase transformation occurred with a shear band when the TWIP steel is processed by 10-revolutions HPT, evidenced by the formation of $M_{23}C_6$ carbide marked in a square. The edge of the shear band, where GBs aligned, is indicated by arrows; (b) enlarged TEM images of the square in (a); (c) HRTEM image and FFT of the $M_{23}C_6$ carbide, showing the formation of twins.

rolling at 573 K in the same TWIP steel although high density of dislocation was introduced [41]. Hence, the hydrostatic pressure, large shear stress and the formation of nanostructures provided by HPT crucially promote the phase transformation as well. It has been proposed that the application of high external pressure could remarkably influence the phase equilibrium by reducing the gap of the Gibbs free energies between parent and new phases, while HPT-induced nanostructures significantly increase the overall free energy of the matrix [14,37,51], both of which may make the phase transformation thermodynamically easier. Moreover, the high shear stress is generally prone to stimulate the transformation by providing additional energy for the nucleation and propagation of new phases [14,37]. These factors may not only prefer the emergence of the phase transformation, but also affect the transformation processes.

It was revealed that the metastable austenite of a TWIP steel could be partially transformed into the typical pearlite during the long-term isothermal aging [53]. However, the austenite finally

decomposed into ferrite and $M_{23}C_6$ carbide rather than cementite in present study, although there was some cementite at early stages of the phase transformation. To further identify the nature of the carbide, its atomic structure was analyzed. Fig. 15 (a) shows a typical $\langle 110 \rangle$ high-resolution TEM image of the carbide, and the inset low magnification image exhibits the morphology of the whole carbide particle. Through the FFT [Fig. 15 (b)] and Inverse FFT (IFFT) [Fig. 15 (c)], the atomic scale structure of the carbide outlined in Fig. 15 (d) is consistent with the theoretically calculated lattice structure of $Mn_{23}C_6$ carbide [56], which substantially validates the identification of the carbide. Due to the similar sizes of Fe and Mn atoms, it is difficult to distinguish them in the $M_{23}C_6$ carbide. The APT study revealed that the C content of the carbide is lower than the stoichiometric value of the $M_{23}C_6$. This may be attributed to the partitioning of C from carbide into ferrites during deformation [54], while the C atoms could be readily attracted by the vacancies and dislocations in ferrite resulting in the higher C concentration in severely deformed ferrite than in conventional ferrite [14,54].

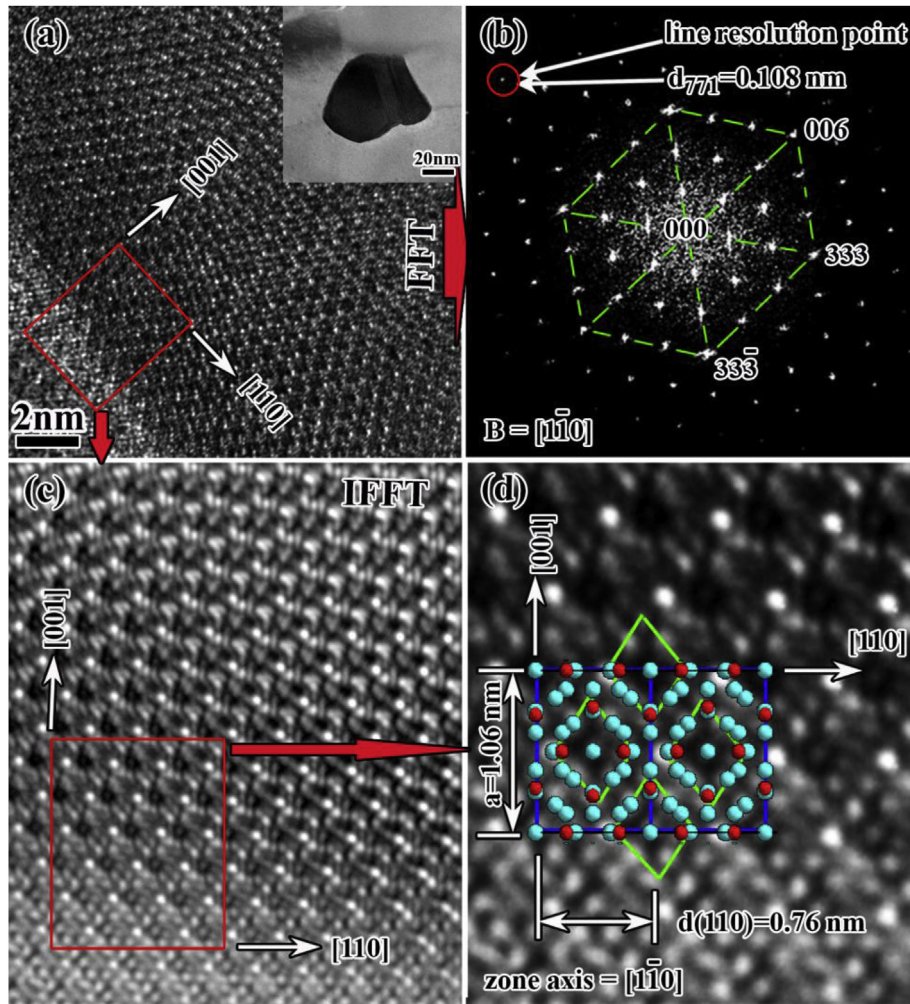


Fig. 15. (a) The low magnification and HRTEM images of the $M_{23}C_6$ carbide; (b) the FFT of (a); (c) the enlarged IFFT image of the rectangle area in (a); (d) the enlarged image the rectangle area in (c) and the theoretical atomic structure of $Mn_{23}C_6$ with Mn atoms in cyan and C atoms in red, which further confirm the identification of $M_{23}C_6$ carbide. (For interpretation of the references to colour in this figure legend, the reader is referred to the web version of this article.)

Concerning that the detailed transformation processes were rather complicated, the reason of low C content in the carbide need further exploration in future.

$M_{23}C_6$ carbides are common in Mo and W-containing steels, low alloy steels, and stainless steels [57–59], while Mn-enriched $M_{23}C_6$ carbides are also detected in high-Mn steels, which involves the extensive diffusion of Mn atoms [60,61]. At the early stages of the phase transformation in present study, since C diffuses much faster than Mn, it is expected that cementite formed in regions where Mn segregation is relatively inconspicuous and $M_{23}C_6$ carbides also nucleated in areas where Mn atoms are substantially segregated. However, cementite disappeared with further deformation and transformation, which may be attributed to the transformation of cementite to $M_{23}C_6$ carbide [57,62]. Both experimental and theoretical studies revealed that the cementite could be evolved into $M_{23}C_6$ through the reaction of $M_3C + \gamma = M_{23}C_6 + \alpha$ [56,62]. Cementite could also be dissolved through C–dislocation interactions during HPT since cementite is unstable when subjected to severe shear deformation [13,14,54]. Accordingly, more $M_{23}C_6$ carbides precipitated owing to the increasingly remarkable segregation of Mn atoms, also accelerated by the plastic deformation [58]. The formation of $M_{23}C_6$ significantly denudes the Mn in the matrix and destabilizes the austenite, leading to simultaneous transformation of austenite to ferrite. Therefore, the diffusion and

segregation of Mn atoms dominantly affect the phase transformation of the TWIP steel during HPT. Similar to the effect of SPD on the precipitation process in Al alloys [63], HPT processing not only stimulates the diffusional phase transformation of the TWIP steel, but also influences the transformation kinetics. In addition, such diffusional phase transformation may be employed to hierarchically manipulate the microstructures through adjusting the processing conditions to design advanced steels with superior mechanical properties.

5. Conclusions

The microstructural evolution and phase transformation of a TWIP steel processed by HPT at 573 K have been systematically studied by recourse to various advanced characterization techniques including XRD, EBSD, TKD, TEM and APT. The results are summarized as follows.

- (1) Because the high processing temperature of 573 K does not favor deformation twinning, the grain refinement process of the TWIP steel was dominated by complex dislocation and GB activities.
- (2) The HPT-induced microstructural evolution and grain refinement of the TWIP steel during HPT can be divided into

four stages: the accumulation of high-density defects within the grains, shear deformation of the GBs, fragmentation of elongated grains, and eventual formation of uniform equiaxed nanograins.

- (3) Diffusional phase transformation, which leads to inhomogeneous compositional distribution, took place at the later stages of deformation. A high density of defects, nanostructures and the HPT processing play crucial roles in promoting the elemental diffusion and transformation.
- (4) During the phase transformation, austenite decomposed finally into ferrite and Mn-riched $M_{23}C_6$ carbides, although cementite formed at the early stages of the transformation. Mn was the dominant element for the transformation kinetics.

Acknowledgments

The authors acknowledge the scientific and technical input and support from the Australian Microscopy & Microanalysis Research Facility node at the University of Sydney. This project was supported by University of Sydney Postdoctoral Research Fellowship, the Australian Research Council (Grant No. DP150101121). Dr. R.D. Liu and X. Wang of Ansteel are acknowledged for providing the TWIP steel samples.

References

- [1] K.S. Kumar, H. Van Swygenhoven, S. Suresh, Mechanical behavior of nanocrystalline metals and alloys, *Acta Mater.* 51 (2003) 5743–5774.
- [2] M.A. Meyers, A. Mishra, D.J. Benson, Mechanical properties of nanocrystalline materials, *Prog. Mater. Sci.* 51 (2006), 427–556.
- [3] R.Z. Valiev, R.K. Islamgaliev, I.V. Alexandrov, Bulk nanostructured materials from severe plastic deformation, *Prog. Mater. Sci.* 45 (2000) 103–189.
- [4] Y. Estrin, A. Vinogradov, Extreme grain refinement by severe plastic deformation: a wealth of challenging science, *Acta Mater.* 61 (2013) 782–817.
- [5] R.Z. Valiev, Y. Estrin, Z. Horita, T.G. Langdon, M.J. Zehetbauer, Y.T. Zhu, Fundamentals of superior properties in bulk nanoscale materials, *Mater. Res. Lett.* (2015), <http://dx.doi.org/10.1080/21663831.2015.1060543>.
- [6] Y. Iwahashi, Z. Horita, M. Nemoto, T.G. Langdon, An investigation of microstructural evolution during equal-channel angular pressing, *Acta Mater.* 45 (1997) 4733–4741.
- [7] R. Pippin, S. Scheriau, A. Taylor, M. Hafok, A. Hohenwarter, A. Bachmaier, Saturation of fragmentation during severe plastic deformation, *Annu. Rev. Mater. Res.* 40 (2010) 319–343.
- [8] S. Qu, X.H. An, H.J. Yang, C.X. Huang, G. Yang, Q.S. Zang, Z.G. Wang, S.D. Wu, Z.F. Zhang, Microstructural evolution and mechanical properties of Cu–Al alloys subjected to equal channel angular pressing, *Acta Mater.* 57 (2009) 1586–1601.
- [9] N.R. Tao, K. Lu, Nanoscale structural refinement via deformation twinning in face-centered cubic metals, *Scr. Mater.* 60 (2009) 1039–1043.
- [10] J.Y. Huang, Y.T. Zhu, H. Jiang, T.C. Lowe, Microstructures and dislocation configurations in nanostructured Cu processed by repetitive corrugation and straightening, *Acta Mater.* 49 (2001) 1497–1505.
- [11] X.H. An, Q.Y. Lin, S.D. Wu, Z.F. Zhang, R.B. Figueiredo, N. Gao, T.G. Langdon, The influence of stacking fault energy on the mechanical properties of nanostructured Cu and Cu–Al alloys processed by high-pressure torsion, *Scr. Mater.* 64 (2011) 954–957.
- [12] X.H. An, Q.Y. Lin, S.D. Wu, Z.F. Zhang, Improved fatigue strengths of nanocrystalline Cu and Cu–Al Alloys, *Mater. Res. Lett.* 3 (2015) 135–141.
- [13] Y. Ivanisenko, W. Lojkowski, R.Z. Valiev, H.J. Fecht, The mechanism of formation of nanostructure and dissolution of cementite in a pearlitic steel during high pressure torsion, *Acta Mater.* 51 (2003) 5555–5570.
- [14] Y. Ivanisenko, I. MacLaren, X. Sauvage, R.Z. Valiev, H.J. Fecht, Shear-induced α – γ transformation in nanoscale Fe–C composite, *Acta Mater.* 54 (2006) 1659–1669.
- [15] N. Li, Y.D. Wang, R. LinPeng, X. Sun, P.K. Liaw, G.L. Wu, L. Wang, H.N. Cai, Localized amorphism after high-strain-rate deformation in TWIP steel, *Acta Mater.* 59 (2011) 6369–6377.
- [16] C. Borchers, C. Garve, M. Tiegel, M. Deutges, A. Herz, K. Edalati, R. Pippin, Z. Horita, R. Kirchheim, Nanocrystalline steel obtained by mechanical alloying of iron and graphite subsequently compacted by high-pressure torsion, *Acta Mater.* 97 (2015) 207–215.
- [17] O. Grässel, L. Krüger, G. Frommeyer, L.W. Meyer, High strength Fe–Mn–(Al, Si) TRIP/TWIP steels development – properties – application, *Int. J. Plast.* 16 (2000) 1391–1409.
- [18] O. Bouaziz, S. Allain, C.P. Scott, P. Cugy, D. Barbier, High manganese austenitic twinning induced plasticity steels: a review of the microstructure properties relationships, *Curr. Opin. Solid State Mater. Sci.* 15 (2011) 141–168.
- [19] I. Gutierrez-Urrutia, D. Raabe, Dislocation and twin substructure evolution during strain hardening of an Fe–22 wt.% Mn–0.6 wt.% C TWIP steel observed by electron channeling contrast imaging, *Acta Mater.* 59 (2011) 6449–6462.
- [20] D.R. Steinmetz, T. Jäpel, B. Wietbrock, P. Eisenlohr, I. Gutierrez-Urrutia, A. Saeed-Akbari, T. Hickel, F. Roters, D. Raabe, Revealing the strain-hardening behavior of twinning-induced plasticity steels: theory, simulations, experiments, *Acta Mater.* 61 (2013) 494–510.
- [21] S.J. Lee, J. Kim, S.N. Kane, B.C. De Cooman, On the origin of dynamic strain aging in twinning-induced plasticity steels, *Acta Mater.* 59 (2011) 6809–6819.
- [22] M.A. Meyers, K.K. Chawala, *Mechanical Behavior of Materials*, Prentice-Hall Inc, New Jersey, 1999.
- [23] S. Curtze, V.T. Kuokkala, Dependence of tensile deformation behavior of TWIP steels on stacking fault energy, temperature and strain rate, *Acta Mater.* 58 (2010) 5129–5141.
- [24] K. Jeong, J.E. Jin, Y.S. Jung, S. Kang, Y.K. Lee, The effects of Si on the mechanical twinning and strain hardening of Fe–18Mn–0.6C twinning – induced plasticity steel, *Acta Mater.* 61 (2013) 3399–3410.
- [25] D.T. Pierce, J.A. Jimenez, J. Bentley, D. Raabe, C. Oskay, J.E. Wittig, The influence of manganese content on the stacking-fault and austenite/ ϵ -martensite interfacial energies in Fe–Mn–(Al–Si) steels investigated by experiment and theory, *Acta Mater.* 68 (2014) 238–253.
- [26] D.T. Pierce, J.A. Jimenez, J. Bentley, D. Raabe, J.E. Wittig, The influence of stacking fault energy on the microstructural and strain – hardening evolution of Fe–Mn–Al–Si steels during tensile deformation, *Acta Mater.* 100 (2015) 178–190.
- [27] L. Bracke, K. Verbeken, L. Kestens, J. Penning, Microstructure and texture evolution during cold rolling and annealing of a high Mn TWIP steel, *Acta Mater.* 57 (2009) 1512–1524.
- [28] Y. Lu, B. Hutchinson, D.A. Molodov, G. Gottstein, Effect of deformation and annealing on the formation and reversion of ϵ -martensite in an Fe–Mn–C alloy, *Acta Mater.* 57 (2009) 3079–3090.
- [29] K. Jeong, J.-E. Jin, Y.-S. Jung, S. Kang, Y.-K. Lee, The effects of Si on the mechanical twinning and strain hardening of Fe–18Mn–0.6C twinning-induced plasticity steel, *Acta Mater.* 61 (2013) 3399–3410.
- [30] I.-C. Jung, B.C. De Cooman, Temperature dependence of the flow stress of Fe–18Mn–0.6C–xAl twinning-induced plasticity steel, *Acta Mater.* 61 (2013) 6724–6735.
- [31] A. Vorhauer, R. Pippin, On the homogeneity of deformation by high pressure torsion, *Scr. Mater.* 51 (2004) 921–925.
- [32] Y. Son, Y.K. Lee, K.T. Park, C.S. Lee, D.H. Shin, Ultrafine grained ferrite martensite dual phase steels fabricated via equal channel angular pressing: microstructure and tensile properties, *Acta Mater.* 53 (2005) 3125–3134.
- [33] J. Zrník, R. Pippin, S. Scheriau, L. Kraus, M. Fujda, Microstructure and mechanical properties of UFG medium carbon steel processed by HPT at increased temperature, *J. Mater. Sci.* 45 (2010) 4822–4826.
- [34] F.K. Yan, G.Z. Liu, N.R. Tao, K. Lu, Strength and ductility of 316L austenitic stainless steel strengthened by nano-scale twin bundles, *Acta Mater.* 60 (2012) 1059–1071.
- [35] Y. Cao, Y.B. Wang, X.H. An, X.Z. Liao, M. Kawasaki, S.P. Ringer, T.G. Langdon, Y.T. Zhu, Concurrent microstructural evolution of ferrite and austenite in a duplex stainless steel processed by high-pressure torsion, *Acta Mater.* 63 (2014) 16–29.
- [36] Z. Yanushkevich, A. Belyakov, R. Kaibyshev, Microstructural evolution of a 304-type austenitic stainless steel during rolling at temperatures of 773–1273 K, *Acta Mater.* 82 (2015) 244–254.
- [37] M.S. Matoso, R.B. Figueiredo, M. Kawasaki, D.B. Santos, T.G. Langdon, Processing a twinning-induced plasticity steel by high-pressure torsion, *Scr. Mater.* 67 (2012) 649–652.
- [38] I.B. Timokhina, A. Medvedev, R. Lapovok, Severe plastic deformation of a TWIP steel, *Mater. Sci. Eng. A* 593 (2014) 163–169.
- [39] A.P. Zhilyaev, T.G. Langdon, Using high-pressure torsion for metal processing: fundamentals and applications, *Prog. Mater. Sci.* 53 (2008) 893–979.
- [40] Z.Y. Liang, X. Wang, W. Huang, M.X. Huang, Strain rate sensitivity and evolution of dislocations and twins in a twinning-induced plasticity steel, *Acta Mater.* 88 (2015) 170–179.
- [41] Z.Y. Liang, Y.Z. Li, M.X. Huang, The respective hardening contributions of dislocations and twins to the flow stress of a twinning-induced plasticity steel, *Scr. Mater.* 112 (2016) 28–31.
- [42] P.W. Trimby, Y. Cao, Z.B. Chen, S. Han, K.J. Hemker, J.S. Lian, X.Z. Liao, P. Rottmann, S. Samudrala, J.L. Sun, J.T. Wang, J. Wheeler, J.M. Cairney, Characterizing deformed ultrafine-grained and nanocrystalline materials using transmission Kikuchi diffraction in a scanning electron microscope, *Acta Mater.* 62 (2014) 69–80.
- [43] X.H. An, S.D. Wu, Z.F. Zhang, R.B. Figueiredo, N. Gao, T.G. Langdon, Evolution of microstructural homogeneity in copper processed by high-pressure torsion, *Scr. Mater.* 63 (2010) 560–563.
- [44] I. Gutierrez-Urrutia, S. Zaefferer, D. Raabe, The effect of grain size and grain orientation on deformation twinning in a Fe–22 wt.%Mn–0.6wt.%C TWIP steel, *Mater. Sci. Eng. A* 527 (2010) 3552–3560.
- [45] H. Beladi, I.B. Timokhina, Y. Estrin, J. Kim, B.C. De Cooman, S.K. Kim, Orientation dependence of twinning and strain hardening behaviour of a high manganese twinning induced plasticity steel with polycrystalline structure, *Acta Mater.* 59 (2011) 7787–7799.

- [46] X.H. An, Q.Y. Lin, S.D. Wu, Z.F. Zhang, R.B. Figueiredo, N. Gao, T.G. Langdon, Significance of stacking fault energy on microstructural evolution in Cu and Cu–Al alloys processed by high-pressure torsion, *Philos. Mag.* 91 (2011) 3307–3326.
- [47] Y.T. Zhu, X.Z. Liao, X.L. Wu, Deformation twinning in nanocrystalline materials, *Prog. Mater. Sci.* 57 (2012) 1–62.
- [48] X.H. An, S.M. Zhu, Y. Cao, M. Kawasaki, X.Z. Liao, S.R. Ringer, J.F. Nie, T.G. Langdon, Y.T. Zhu, Atomic-scale investigation of interface-facilitated deformation twinning in severely deformed Cu–Ag nanolamellar composites, *App. Phys. Lett.* 107 (2015) 011901.
- [49] Y.J. Li, P. Choi, S. Goto, C. Borchers, D. Raabe, R. Kirchheim, Evolution of strength and microstructure during annealing of heavily cold-drawn 6.3 GPa hypereutectoid pearlitic steel wire, *Acta Mater.* 60 (2012) 4005–4016.
- [50] Y.J. Li, A. Kostka, P. Choi, S. Goto, D. Ponge, R. Kirchheim, D. Raabe, Mechanisms of subgrain coarsening and its effect on the mechanical properties of carbon-supersaturated nanocrystalline hypereutectoid steel, *Acta Mater.* 84 (2015) 110–123.
- [51] X.H. An, S.D. Wu, Z.G. Wang, Z.F. Zhang, Enhanced cyclic deformation responses of ultrafine-grained Cu and nanocrystalline Cu–Al alloys, *Acta Mater.* 74 (2014) 200–214.
- [52] D.A. Porter, K.E. Easterling, *Phase Transformations in Metals and Alloys*, CRC Press, New York, 2004.
- [53] R.T. van Tol, L. Zhao, J. Sietsma, Kinetics of austenite decomposition in manganese-based steel, *Acta Mater.* 64 (2014) 33–40.
- [54] Y.J. Li, P. Choi, C. Borchers, S. Westerkamp, S. Goto, D. Raabe, R. Kirchheim, Atomic-scale mechanisms of deformation-induced cementite decomposition in pearlite, *Acta Mater.* 59 (2011) 3965–3977.
- [55] M. Kuzmina, M. Herbig, D. Ponge, S. Sandlöbes, D. Raabe, Linear complexions: confined chemical and structural states at dislocations, *Science* 349 (2015) 1080–1083.
- [56] J.Y. Xie, L.D. Teng, N.X. Chen, S. Seetharaman, Atomistic simulation on the structural properties and phase stability for Cr₂₃C₆ and Mn₂₃C₆, *J. Alloys Compd.* 420 (2006) 269–272.
- [57] A. Inoue, T. Masumoto, Carbide reactions (M₃C->M₇C₃->M₂₃C₆->M₆C) during tempering of rapidly solidified high carbon Cr–W and Cr–Mo steels, *Metall. Trans. A* 11 (1980) 739–747.
- [58] S.M. Hong, M.Y. Kim, D.J. Min, K.H. Lee, J.H. Shim, D.I. Kim, J.Y. Suh, W.S. Jung, I.S. Choi, Unraveling the origin of strain-induced precipitation of M₂₃C₆ in the plastically deformed 347 Austenite stainless steel, *Mater. Char.* 94 (2014) 7–13.
- [59] M.I. Isik, A. Kostka, V.A. Yardley, K.G. Pradeep, M.J. Duarte, P.P. Choi, D. Raabe, G. Eggeler, The nucleation of Mo-rich Laves phase particles adjacent to M₂₃C₆ micrograin boundary carbides in 12% Cr tempered martensite ferritic steels, *Acta Mater.* 90 (2015) 94–104.
- [60] Y.L. Lin, C.P. Chou, M₂₃C₆ Carbide in an Fe–26.6Mn–8.8Al–0.61C alloy, *Scr. Metall. Mater.* 27 (1992) 67–70.
- [61] L.M. Roncery, S. Weber, W. Theisen, Nucleation and precipitation kinetics of M₂₃C₆ and M₂N in an Fe–Mn–Cr–C–N austenitic matrix and their relationship with the sensitization phenomenon, *Acta Mater.* 59 (2011) 6275–6286.
- [62] D. Djurovic, B. Hallstedt, J.V. Appen, R. Dronskowski, Thermodynamic assessment of the Fe–Mn–C system, *Calphad* 35 (2011) 479–491.
- [63] G. Sha, Y.B. Wang, X.Z. Liao, Z.C. Duan, S.P. Ringer, T.G. Langdon, Influence of equal-channel angular pressing on precipitation in an Al–Zn–Mg–Cu alloy, *Acta Mater.* 57 (2009) 3123–3132.